Theoretical prediction of radiation pressure force exerted on a spheroid by an arbitrarily shaped beam

Feng Xu
Institute of Particle and Two-phase Flow Measurement Technology, University of Shanghai for Science and Technology, 516 Jungong Rd., Shanghai 200093, China
and UMR 6614/CORIA CNRS, Université et INSA de Rouen, Site du Madrillet, Avenue de l'Université, BP12, 76801 Saint Etienne du Rouvray, France

Kuanfang Ren and Gérard Gouesbet
UMR 6614/CORIA CNRS, Université et INSA de Rouen, Site du Madrillet, Avenue de l'Université, BP12, 76801 Saint Etienne du Rouvray, France

Xiaoshu Cai
Institute of Particle and Two-phase Flow Measurement Technology, University of Shanghai for Science and Technology, 516 Jungong Rd., Shanghai 200093, China

Gérard Gréhan
UMR 6614/CORIA CNRS, Université et INSA de Rouen, Site du Madrillet, Avenue de l'Université, BP12, 76801 Saint Etienne du Rouvray, France

(Received 15 August 2006; revised manuscript received 24 November 2006; published 23 February 2007)

A rigorous theory is developed to predict the radiation pressure force (RPF) exerted on a spheroid by an arbitrarily oriented and located shaped beam. Analytical expressions of RPF are derived for a homogeneous spheroid, which can be prolate or oblate, transparent or absorbing. Exemplifying calculations are performed and RPF calculations for spheroids are compared to RPF calculations for spheres. The "Optical Stretcher" is also numerically simulated to study the RPF exerted on a red blood cell during its deformation.

DOI: 10.1103/PhysRevE.75.026613 PACS number(s): 42.25.Fx, 87.80.Cc

I. INTRODUCTION

On the basis of the pioneering work of Ashkin and his co-workers [1–5], optical trapping has found more and more applications in the fields of physics and biology during the last several decades [6,7]. In principle, under the action of the radiation pressure force (RPF) generated by the tightly focused laser beams through a high-numerical-aperture (HNA), small particles can be trapped and moved with the beam to a prescribed location. Theories for RPF computations for a homogeneous spherical particle have also been developed by using different approaches. With respect to the ratio of the particle size over the incident wavelength, two extreme regimes can be distinguished. When the particle is much larger than the wavelength, typically $d/\lambda > 10$, the ray optics regime is concerned and geometrical optics can be employed for RPF predictions [8–18]. Conversely, when it is much smaller than the wavelength ($d \ll \lambda$), the Rayleigh regime is concerned and RPF can be decomposed into scattering and gradient contributions, which can be calculated by using the Rayleigh-Debye theory [19–22]. By taking into account the second-order scattering terms and expanding the incident field into a plane wave spectrum, the validity range of the Rayleigh theory has been extended by Rohrbach *et al.* to particle sizes as large $\sim 0.7\lambda$ [23]. In order to cover the whole range of d/λ, the rigorous electromagnetic theory has been developed for the sphere, in which the solution to Maxwell's equations is found by applying well-known boundary conditions. In such a theory, it is primarily necessary to expand the incident beam in spherical coordinates. Kim and Lee used the complex-source-point method to expand the incident fields [24], Barton combined the particle's geometry with the incident fields and used the surface integral method [25], while Gouesbet *et al.* developed the generalized Lorenz-Mie theory (GLMT) [26] which employs a set of beam shape coefficients (BSCs) to describe the incident beam. Numerical applications of GLMT for spherical particles are available from Ref. [27] and the references therein. Also, in order to simulate the situation of realistic measurements, Lock has applied the GLMT to the study of RPF exerted on a sphere by a tightly focused, truncated and aberrated beam [28,29].

Compared to all these theoretical efforts on the RPF calculation for spherical particles, much less work on the RPF prediction for nonspherical particles has been reported. To our knowledge, only radiation forces and torques exerted on cylindrical particles, ring-shaped particles and a regularly shaped micromotor have been studied by means of geometrical optics [30–33]. Indeed, the RPF predictions for nonspherical particles are not trivial but are important since, in many cases particles for optical trapping cannot be well modeled by spheres, e.g., human sperm [34], genome [35], red blood cells [36], or many other micro-organism cells [37]. Even for spherical particles, once they are not rigid, distortion may take place under the action of the RPF [38–40]. For example, it has been experimentally found [41] that under the action of two counter-propagating laser beams (the "Optical Stretcher"), the shape of a soft biological cell is

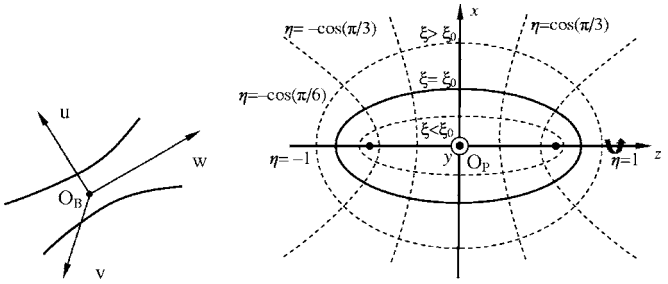

FIG. 1. Coordinates system: O_B-*uvw* is for the incident shaped beam and O_P-*xyz* is for the spheroid.

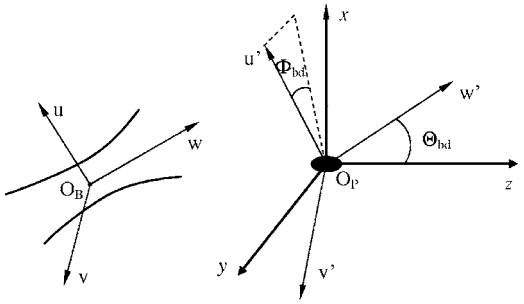

FIG. 2. Geometry of Cartesian coordinates of the beam and spheroid. O_P-*xyz* is the coordinate system of the spheroid and O_P-$u'v'w'$ is translated from the beam coordinates O_B-*uvw* having the origin O_B located at (x_0, y_0, z_0) in O_P-*xyz*.

deformed from spherical to spheroidal. In this case, as well as in some other practical situations, particles used for optical trapping can be more appropriately modeled by spheroids.

Although the variable-separation-based electromagnetic theories for the plane wave or shaped beam scattering by a spheroidal particle have been developed by Asano and Yamamoto [42], Barton [43], and Han *et al.* [44,45], their object was to study the near-or far-field scatterings. RPF was not considered. Relying on our previous work [46] on the study of spheroidal particle scattering for an arbitrarily shaped beam with arbitrary location and orientation in the coordinate system of the particle, this paper provides the analytical expressions and the exemplifying calculations for the RPF exerted on a spheroid.

Instead of using the spheroidal surface integral to describe the beam, [43], we expand the incident fields in terms of infinite series of spheroidal vector wave functions $(\mathbf{M}_{mn}, \mathbf{N}_{mn})$ multiplied by a set of BSCs in spheroidal coordinates ("spheroidal BSCs"), $G^m_{n,TE}$ and $G^m_{n,TM}$. Such a feature provides the possibility to obtain the analytical expressions of the RPF, as done for a spherical particle illuminated by an arbitrarily shaped beam, which is evaluated by the BSCs in spherical coordinates ("spherical BSCs"), $g^m_{n,TE}$ and $g^m_{n,TM}$ [26].

The paper is organized as follows: a general theory is introduced in Sec. II. Comparisons of RPF exerted on a spheroid to that on a sphere and a numerical simulation of the "Optical Stretcher" are given in Sec. III, followed by a conclusion in Sec. IV.

II. THEORY

We consider a monochromatic, arbitrarily oriented and shaped beam whose electric field is linearly polarized in the *u* direction at the waist in its own Cartesian coordinates O_B-*uuw*. It is incident on a spheroid of semimajor axis length *a* and semiminor axis length *b* (Fig. 1). The time-dependent part of the electromagnetic fields of the beam is assumed to be $\exp(-i\omega t)$, where ω denotes the angular frequency of the beam. The particle is surrounded by a homogeneous, nonmagnetic and lossless medium. After a coordinate translation, the beam center O_B can be moved to particle center O_P so that O_P-$u'v'w'$ is brought in. Taking the symmetrical axis of the spheroid as the *z* axis, we make the *x* axis of the Cartesian coordinates of the particle lying in the plane formed by the w' and *z* axes. In this way the Cartesian coordinates of the particle O_P-*uvw* is determined. As indicated by Fig. 2, the two coordinate systems can be related by two angles. One is the incidence angle Θ_{bd} indicating the propagation direction of the beam along the positive *w* axis relative to the O_P-*yz* plane, the other one is the polarization angle Φ_{bd} indicating the polarization direction of the incident-electric-field (along the *u* axis) relative to the O_P-*xz* plane. These two angles are used to evaluate the spheroidal BSCs [46]. Additionally, O_B is assumed to locate at (x_0, y_0, z_0) in O_P-*xyz*.

In this section we only discuss the RPF calculation for the prolate spheroid, since all the equations and expressions pertaining to the prolate spheroidal coordinates can be converted to their counterparts in the oblate system through a replacement $\begin{cases} c \to -ic \\ \xi \to i\xi \end{cases}$, in which $c=kf$, *k* being the wave number, *f* being the semifocal length of the spheroid and ξ being the spheroidal radial coordinate.

A. Description of the incident and scattered fields

As described in the spheroidal scattering theory developed in the previous paper [46], the incident electromagnetic fields $(\mathbf{E}^{(i)}, \mathbf{H}^{(i)})$ and the scattered ones $(\mathbf{E}^{(s)}, \mathbf{H}^{(s)})$ in the spheroidal coordinates (ξ, η, ϕ) can be expanded in terms of the spheroidal vector wave functions $(\mathbf{M}^{(i)}_{mn}, \mathbf{N}^{(i)}_{mn})$ and $(\mathbf{M}^{(s)}_{mn}, \mathbf{N}^{(s)}_{mn})$ as follows:

$$\mathbf{E}^{(i)} = \sum_{m=-\infty}^{\infty} \sum_{n=|m|, n\neq 0}^{\infty} i^{n+1} [iG^m_{n,TE} \mathbf{M}^{(i)}_{mn}(c_1; \xi, \eta, \phi) + G^m_{n,TM} \mathbf{N}^{(i)}_{mn} \times (c_1; \xi, \eta, \phi)], \quad (1)$$

$$\mathbf{H}^{(i)} = -\frac{ik_1}{\omega\mu_0} \sum_{m=-\infty}^{\infty} \sum_{n=|m|, n\neq 0}^{\infty} i^{n+1} [G^m_{n,TM} \mathbf{M}^{(i)}_{mn}(c_1; \xi, \eta, \phi) + iG^m_{n,TE} \mathbf{N}^{(i)}_{mn}(c_1; \xi, \eta, \phi)], \quad (2)$$

$$\mathbf{E}^{(s)} = \sum_{m=-\infty}^{\infty} \sum_{n=|m|, n\neq 0}^{\infty} i^{n+1} [B^m_n \mathbf{M}^{(s)}_{mn}(c_1; \xi, \eta, \phi) + A^m_n \mathbf{N}^{(s)}_{mn} \times (c_1; \xi, \eta, \phi)], \quad (3)$$

$$\mathbf{H}^{(s)} = -\frac{ik_1}{\omega\mu_0}\sum_{m=-\infty}^{\infty}\sum_{n=|m|,n\neq 0}^{\infty} i^{n+1}[A_n^m\mathbf{M}_{mn}^{(s)}(c_1;\xi,\eta,\phi) + B_n^m\mathbf{N}_{mn}^{(s)} \times(c_1;\xi,\eta,\phi)], \tag{4}$$

where μ_0 is the permeability of the free space, c_1 is the size parameter of the spheroid and is identical to $k_1 f$ (k_1 being the wave number in the medium), and (A_n^m, B_n^m) are the scattering coefficients. Via the following formulas, the spheroidal BSCs $(G_{n,TE}^m, G_{n,TM}^m)$ can be determined from their counterparts $(g_{n,TE}^m, g_{n,TM}^m)$ in the spherical coordinates (r,θ,ϕ), which corresponds to the same particle Cartesian coordinates O_P-xyz as the spheroidal coordinates (ξ,η,ϕ),

$$G_{n,TE}^m = \frac{1}{N_{mn}}\sum_{r=0,1}^{\infty}{}' g_{r+|m|,TE}^m \frac{2(r+2|m|)!}{(r+|m|)(r+|m|+1)r!} d_r^{|m|n}(c_1), \tag{5}$$

$$G_{n,TM}^m = \frac{1}{N_{mn}}\sum_{r=0,1}^{\infty}{}' g_{r+|m|,TM}^m \frac{2(r+2|m|)!}{(r+|m|)(r+|m|+1)r!} d_r^{|m|n}(c_1), \tag{6}$$

where the prime sign in the sum symbol indicates a summation which starts from $\{{}^0_1\}$ over the $\{{}^{\text{even}}_{\text{odd}}\}$ indices of r when $(n-m)$ is $\{{}^{\text{even}}_{\text{odd}}\}$ and $d_r^{|m|n}(c_1)$ are the expansion coefficients of the angular functions S_{mn} in the prolate spheroidal coordinates normalized by N_{mn},

$$N_{mn} = \sum_{r=0,1}^{\infty}{}' \frac{2(r+2|m|)!}{(2r+2|m|+1)r!}[d_r^{|m|n}(c_1)]^2. \tag{7}$$

For a given set of incidence and polarization angles (Θ_{bd}, Φ_{bd}), the spherical BSCs in Eqs. (5) and (6), $g_{n,TE}^m$ and $g_{n,TM}^m$ can be evaluated [46] from the following triple integrals on the r components of the incident electromagnetic fields, $E_r^{(i)}$ and $H_r^{(i)}$, in spherical coordinates,

$$g_{n,TM}^m = \frac{(2n+1)(-i)^{n+1}}{2\pi^2}\frac{(n-|m|)!}{(n+|m|)!}\int_0^{\infty} k_1 r z_n(k_1 r)\int_0^{2\pi} \exp(-im\phi)\int_0^{\pi}\frac{E_r^{(i)}(r,\theta,\phi)}{E_0}P_n^{|m|}(\cos\theta)\sin\theta d\theta d\phi d(k_1 r), \tag{8}$$

$$g_{n,TE}^m = \frac{(2n+1)(-i)^{n+1}}{2\pi^2}\frac{(n-|m|)!}{(n+|m|)!}\int_0^{\infty} k_1 r z_n(k_1 r)\int_0^{2\pi} \exp(-im\phi)\int_0^{\pi}\frac{H_r^{(i)}(r,\theta,\phi)}{H_0}P_n^{|m|}(\cos\theta)\sin\theta d\theta d\phi d(k_1 r), \tag{9}$$

where P_n^m are the associated Legendre functions of the first kind with Ferrer's definition [47].

Once the spheroidal BSCs are obtained, the scattering coefficients (A_n^m, B_n^m) can be determined [46] from the boundary conditions ensuring the continuity of the tangential components of the electric and magnetic vectors across the surface of the spheroid $\xi=\xi_0$.

It is necessary to note that in Eqs. (1) and (2), $\mathbf{M}_{mn}^{(i)}$ and $\mathbf{N}_{mn}^{(i)}$, the spheroidal vector functions describing the incident fields are associated with $R_{mn}^{(1)}$, the radial functions of the first kind [48] which are finite at the origin of the spheroidal coordinates ($c\xi=0$). In Eqs. (3) and (4), $\mathbf{M}_{mn}^{(3)}$ and $\mathbf{N}_{mn}^{(3)}$, the spheroidal vector functions describing the scattered field are associated with $R_{mn}^{(3)}$, the radial functions of the third kind [48] ensuring us that the scattered wave becomes a diverging spherical wave when the spheroidal radial coordinate ξ tends to infinity.

B. Radiation pressure

The RPF exerted by the beam on the particle is proportional to the net momentum removed from the incident beam. If we use the radiation pressure cross sections (RPCS) $C_{pr,x}$, $C_{pr,y}$, and $C_{pr,z}$, to characterize the transverse (along the x and y axes) and longitudinal (along the z axis) components of RPF, respectively, they can be related to the integral of the absorption cross section, C_{abs}, by [26]

$$C_{pr,x} = c_m F_x = \overline{\sin\theta\cos\phi} C_{abs}, \tag{10}$$

$$C_{pr,y} = c_m F_y = \overline{\sin\theta\sin\phi} C_{abs}, \tag{11}$$

$$C_{pr,z} = c_m F_z = \overline{\cos\theta} C_{abs}, \tag{12}$$

where c_m denotes the light speed in the surrounding medium and F_x, F_y, and F_z denote the three components of RPF along the x, y, and z axes, respectively.

Since the time-averaged Poynting vector $\mathbf{S}$ can be obtained from the incident and scattered electromagnetic fields outside the particle as follows [49]:

$$\mathbf{S} = \frac{c_m}{8\pi}(\mathbf{E}^{(i)}\times\mathbf{H}^{(i),*} + \mathbf{E}^{(s)}\times\mathbf{H}^{(s),*} + \mathbf{E}^{(i)}\times\mathbf{H}^{(s),*} + \mathbf{E}^{(s)} \times\mathbf{H}^{(i),*}), \tag{13}$$

and the energy absorbed by the particle is minus the integral result of the Poynting vector over a closed surface around the particle, we have the following integral for the absorption cross section:

$$C_{abs} = -\mathrm{Re}\left\{\int\int_{\Sigma}(\mathbf{E}^{(s)}\times\mathbf{H}^{(s),*} + \mathbf{E}^{(i)}\times\mathbf{H}^{(s),*} + \mathbf{E}^{(s)} \times\mathbf{H}^{(i),*})\cdot\mathbf{n}dS\right\}, \tag{14}$$

where S may denote a spherical surface of a sphere with radius r, containing the particle and centered at a point inside the particle, $\mathbf{n}$ is the unit outward normal with respect to S, Re denotes the real part of the integral values and the asterisk denotes the complex conjugate. Note that the integral value

of the first term of the Poynting vector [Eq. (13)] over a closed surface of the particle is zero.

When the spheroidal radial coordinate ξ tends to infinity ($\xi \to \infty$), the spheroidal surface characterized by the spheroidal radial coordinate ξ becomes a spherical one ($c\xi$ tends to kr and η tends to $\cos\theta$) and the radial components of the spheroidal vector wave functions become zero. Using such a spherical surface to perform the integral of Eq. (14), we have the following integral expression for C_{abs}:

$$C_{\text{abs}} = \int_0^{\pi}\int_0^{2\pi} \frac{1}{2}\,\text{Re}(E_\phi^{(i)}H_\eta^{(s)} + E_\phi^{(s)}H_\eta^{(i)*} - E_\eta^{(i)}H_\phi^{(s)} - E_\eta^{(s)}H_\phi^{(i)*} - E_\eta^{(s)}H_\phi^{(s)*} + E_\phi^{(s)}H_\eta^{(s)*})r^2 \sin\theta d\theta d\phi. \quad (15)$$

Substituting Eq. (15) into Eqs. (10)–(12) yields the following expressions of RPCS:

$$C_{\text{pr},x} = \int_0^{\pi}\int_0^{2\pi} \frac{1}{2}\,\text{Re}(E_\phi^{(i)}H_\eta^{(s)} + E_\phi^{(s)}H_\eta^{(i)*} - E_\eta^{(i)}H_\phi^{(s)} - E_\eta^{(s)}H_\phi^{(i)*} - E_\eta^{(s)}H_\phi^{(s)*} + E_\phi^{(s)}H_\eta^{(s)*})r^2 \sin^2\theta\cos\phi d\theta d\phi, \quad (16)$$

$$C_{\text{pr},y} = \int_0^{\pi}\int_0^{2\pi} \frac{1}{2}\,\text{Re}(E_\phi^{(i)}H_\eta^{(s)} + E_\phi^{(s)}H_\eta^{(i)*} - E_\eta^{(i)}H_\phi^{(s)} - E_\eta^{(s)}H_\phi^{(i)*} - E_\eta^{(s)}H_\phi^{(s)*} + E_\phi^{(s)}H_\eta^{(s)*})r^2 \sin^2\theta\sin\phi d\theta d\phi, \quad (17)$$

$$C_{\text{pr},z} = \int_0^{\pi}\int_0^{2\pi} \frac{1}{2}\,\text{Re}(E_\phi^{(i)}H_\eta^{(s)} + E_\phi^{(s)}H_\eta^{(i)*} - E_\eta^{(i)}H_\phi^{(s)} - E_\eta^{(s)}H_\phi^{(i)*} - E_\eta^{(s)}H_\phi^{(s)*} + E_\phi^{(s)}H_\eta^{(s)*})r^2 \sin\theta\cos\theta d\theta d\phi. \quad (18)$$

Moreover, the η and ϕ components of the spheroidal vector wave functions describing the incident and scattered waves have the following asymptotic behaviors as $\xi \to \infty$:

$$M_{mn,\eta}^{(i)} = -\frac{1}{2}\left[(-i)^n\frac{e^{ik_1r}}{k_1r} - i^n\frac{e^{-ik_1r}}{k_1r}\right]\frac{mS_{|m|n}(c_1,\cos\theta)}{\sin\theta}\exp(im\phi), \quad (19)$$

$$M_{mn,\phi}^{(i)} = -\frac{1}{2}\left[(-i)^{n+1}\frac{e^{ik_1r}}{k_1r} + i^{n+1}\frac{e^{-ik_1r}}{k_1r}\right]\frac{dS_{|m|n}(c_1,\cos\theta)}{d\theta}\exp(im\phi), \quad (20)$$

$$N_{mn,\eta}^{(i)} = -\frac{1}{2}\left[(-i)^n\frac{e^{ik_1r}}{k_1r} - i^n\frac{e^{-ik_1r}}{k_1r}\right]\frac{dS_{|m|n}(c_1,\cos\theta)}{d\theta}\exp(im\phi), \quad (21)$$

$$N_{mn,\phi}^{(i)} = -\frac{1}{2}\left[(-i)^{n+1}\frac{e^{ik_1r}}{k_1r} + i^{n+1}\frac{e^{-ik_1r}}{k_1r}\right]\frac{mS_{|m|n}(c_1,\cos\theta)}{\sin\theta}\exp(im\phi), \quad (22)$$

$$M_{mn,\eta}^{(s)} = -(-i)^n\frac{e^{ik_1r}}{k_1r}\frac{mS_{|m|n}(c_1,\cos\theta)}{\sin\theta}\exp(im\phi), \quad (23)$$

$$M_{mn,\phi}^{(s)} = -(-i)^{n+1}\frac{e^{ik_1r}}{k_1r}\left[\frac{dS_{|m|n}(c_1,\cos\theta)}{d\theta}\right]\exp(im\phi), \quad (24)$$

$$N_{mn,\eta}^{(s)} = -(-i)^n\frac{e^{ik_1r}}{k_1r}\frac{dS_{|m|n}(c_1,\cos\theta)}{d\theta}\exp(im\phi), \quad (25)$$

$$N_{mn,\phi}^{(s)} = -(-i)^{n+1}\frac{e^{ik_1r}}{k_1r}\frac{mS_{|m|n}(c_1,\cos\theta)}{\sin\theta}\exp(im\phi), \quad (26)$$

where the angular functions S_{mn} are calculated from the following infinite series of the Legendre functions [48],

$$S_{mn}(c_1,\cos\theta) = \sum_{r=0,1}^{\infty}{}' d_r^{mn}(c_1)P_{m+r}^m(\cos\theta). \quad (27)$$

Substituting Eqs. (19)–(26) into the corresponding η and ϕ components of the incident and scattered fields expressed by Eqs. (1)–(4), using Eqs. (16)–(18) and invoking the orthogonality relations listed in the Appendix for the generalized angular functions $\frac{S_{mn}(c_1,\cos\theta)}{\sin\theta}$, their derivatives $\frac{dS_{mn}(c_1,\cos\theta)}{d\theta}$, as well as the exponentials $\exp(im\phi)$, the following analytical expressions of RPCS can be obtained after a great deal of algebra:

$$C_{pr,x} = \frac{\lambda^2}{4\pi}\sum_{p=1}^{+\infty}\sum_{n=p-1\neq 0}^{+\infty}\sum_{n'=p}^{+\infty}\text{Re}[L_{nn'}^{p-1}(2U_{nn'}^{p-1} - S_{nn'}^{p-1}) + L_{n'n}^{-p}(2U_{n'n}^{-p} - S_{n'n}^{-p}) + iM_{nn'}^{p-1}(2V_{nn'}^{p-1} - T_{nn'}^{p-1}) + iM_{n'n}^{-p}(2V_{n'n}^{-p} - T_{n'n}^{-p})], \quad (28)$$

$$C_{pr,y} = \frac{\lambda^2}{4\pi}\sum_{p=1}^{+\infty}\sum_{n=p-1\neq 0}^{+\infty}\sum_{n'=p}^{+\infty}\text{Im}[L_{nn'}^{p-1}(2U_{nn'}^{p-1} - S_{nn'}^{p-1}) + L_{n'n}^{-p}(2U_{n'n}^{-p} - S_{n'n}^{-p}) + iM_{nn'}^{p-1}(2V_{nn'}^{p-1} - T_{nn'}^{p-1}) + iM_{n'n}^{-p}(2V_{n'n}^{-p} - T_{n'n}^{-p})], \quad (29)$$

$$C_{pr,z} = \frac{\lambda^2}{4\pi}\sum_{p=-\infty}^{+\infty}\sum_{n=|p|\neq 0}^{+\infty}\sum_{n'=|p|\neq 0}^{+\infty}\text{Re}[J_{nn'}^p(O_{nn'}^p + P_{nn'}^p) + ipK_{nn'}^p(Q_{nn'}^p - R_{nn'}^p)], \quad (30)$$

where $J_{nn'}^p - M_{nn'}^p$ are expressed by Eqs. (A9)–(A12) in the Appendix and $O_{nn'}^p - V_{nn'}^p$ are given by

$$O_{nn'}^{p} = G_{n,TM}^{p} A_{n'}^{p,*} + G_{n',TM}^{p,*} A_{n}^{p} - 2A_{n}^{p} A_{n'}^{p,*}, \tag{31}$$

$$P_{nn'}^{p} = G_{n,TE}^{p} B_{n'}^{p,*} + G_{n',TE}^{p,*} B_{n}^{p} - 2B_{n}^{p} B_{n'}^{p,*}, \tag{32}$$

$$Q_{nn'}^{p} = G_{n,TE}^{p} A_{n'}^{p,*} + G_{n',TM}^{p,*} B_{n}^{p} - 2A_{n'}^{p,*} B_{n}^{p}, \tag{33}$$

$$R_{nn'}^{p} = G_{n,TM}^{p} B_{n'}^{p,*} + G_{n',TE}^{p,*} A_{n}^{p} - 2A_{n}^{p} B_{n'}^{p,*}, \tag{34}$$

$$S_{nn'}^{p} = A_{n}^{p} G_{n',TM}^{p+1,*} + A_{n'}^{p+1,*} G_{n,TM}^{p} + B_{n}^{p} G_{n',TE}^{p+1,*} + B_{n'}^{p+1,*} G_{n,TE}^{p}, \tag{35}$$

$$T_{nn'}^{p} = B_{n}^{p} G_{n',TM}^{p+1,*} + B_{n'}^{p+1,*} G_{n,TE}^{p} - A_{n}^{p} G_{n',TE}^{p+1,*} - A_{n'}^{p+1,*} G_{n,TM}^{p}, \tag{36}$$

$$U_{nn'}^{p} = A_{n}^{p} A_{n'}^{p+1,*} + B_{n}^{p} B_{n'}^{p+1,*}, \tag{37}$$

$$V_{nn'}^{p} = A_{n'}^{p+1,*} B_{n}^{p} - A_{n}^{p} B_{n'}^{p+1,*}. \tag{38}$$

III. NUMERICAL CALCULATIONS

Relying on the theory developed in the preceding part of the paper, this section presents some numerical results. Except for the red blood cell levitated by the beam from a sapphire laser used for the numerical simulation of the "Optical Stretcher" in Sec. III B, the particle used for calculation in the remaining parts is the slightly volatile silicone oil of refractive index $\hat{m}=1.5$ [50]. It is levitated in the air by the beam from an argon-ion laser having the wavelength $\lambda_0 = 0.5145$ μm [51].

Since the prolate and oblate spheroids are formed by rotating an ellipse around its major axis, and minor axis respectively, these two axes are the symmetrical axes for the prolate and oblate spheroids, respectively. When the beam propagates parallelly to the symmetrical axis of the spheroid, the end-on incidence is brought in and when it propagates vertically to the symmetrical axis, the side-on incidence is brought in. For the end-on incidence, when using the projection radius R to characterize the projection area of the spheroid, we have $R=b$ for the prolate spheroid and $R=a$ for the oblate one. Such a radius can be related to the size parameter by $c_I = k_I R\sqrt{(a/b)^2 - 1}$ for the prolate spheroid and by $c_I = k_I R\sqrt{1 - 1/(a/b)^2}$ for the oblate one. The influence of the particle size characterized by R on the RPF is to be studied for a given axis ratio a/b. To study RPF in the experiment of the "Optical Stretcher," the RPCS will be calculated for a given volume of a soft and spherical red blood cell (RBC) acted on by two counter-propagating laser beams and deformed to the spheroidal shape. Besides, influences of the incidence and polarization angles as well as the beam center location will also be studied in the present section.

Since the description of the beam is significant for the RPF calculation in some cases [52], here it is necessary to point out that throughout the present section, Davis first order approximation [53] is used to describe the electromagnetic beams. Additionally, because of its high efficiency, the localization approximation method [54,55] is used for BSCs evaluation when the end-on incidence is involved and the electric field of the beam is polarized in the O_P-xz plane ($\Theta_{bd}=\Phi_{bd}=0$). While in other cases, the classical localization principle has been found inapplicable [56], therefore quadrature method [57] is used instead.

A. Radiation pressure force versus particle size

In this section, we predict the radiation pressure exerted on a spheroid by an end-on incident plane wave. Both prolate and oblate spheroids are used for calculation. The results are compared to those obtained by the GLMT for the spherical particle of an exact axis ratio $a/b=1.0$. With the resolution being $\Delta R \sim 2.5\times 10^{-4}$ μm, 8000 equidistant points within the interval 0.1 μm$\leqslant R \leqslant$2.0 μm are used in RPCS calculation, since in such a range it is easier to recognize the position difference of the resonances between a spheroid and a sphere.

As indicated in Fig. 3, when compared to the RPCS curve versus the particle size for the sphere, the RPCS curve for the prolate spheroid of the axis ratio $a/b=1.01$ has a backward and downward shift. Such a shift becomes upward and forward for the oblate spheroid of the same axis ratio. Moreover, these shifts are enlarged when the spheroid deviates more from the sphere, e.g., $a/b=1.1$, as shown by Fig. 4 (note that for the clarity of Fig. 4, the RPCS curves of the prolate and oblate spheroids have been offset by the factors 2×10^{-12} and -2×10^{-12}, respectively). After a careful identification, we can find in Fig. 4 that when the sphere changes to the prolate spheroid, the points A_2, B_2, and C_2 on the RPCS curve shift to A_3, B_3, and C_3, respectively, which implies an inward compression of the RPCS curve of the sphere. In contrast, when the sphere changes to the oblate spheroid, the outward stretching is brought in and in this case the points A_2, B_2, and C_2 are found to shift to A_1, B_1, and C_1, respectively. Comparison of the distance between the two points A_1 and A_2 (or A_2 and A_3) to that between B_1 and B_2 (or B_2 and B_3) shows that large particles have more obvious shift than small ones. Comparison of the RPCS values at the points corresponding to the same order of the resonances shows that the resonance strength is enhanced by the oblate spheroid but is reduced by the prolate one. Comparison of the RPCS curves in Fig. 4 to those in Fig. 3 shows that for the prolate spheroid increasing its axis ratio makes the resonances weaker in strength, narrower in width and more difficult to identify. But for the oblate spheroid, increasing the axis ratio makes the resonances stronger, wider and easier to identify. Besides, as for the spherical particle, increasing the size of the spheroid makes the resonances stronger but narrower.

B. Radiation pressure force versus axis ratio

In the preceding section, we keep constant the axis ratio of the spheroid and discuss the behavior of the RPCS curves versus the particle size. In this section, the volume of the particle is to be given and kept constant during the deforma-

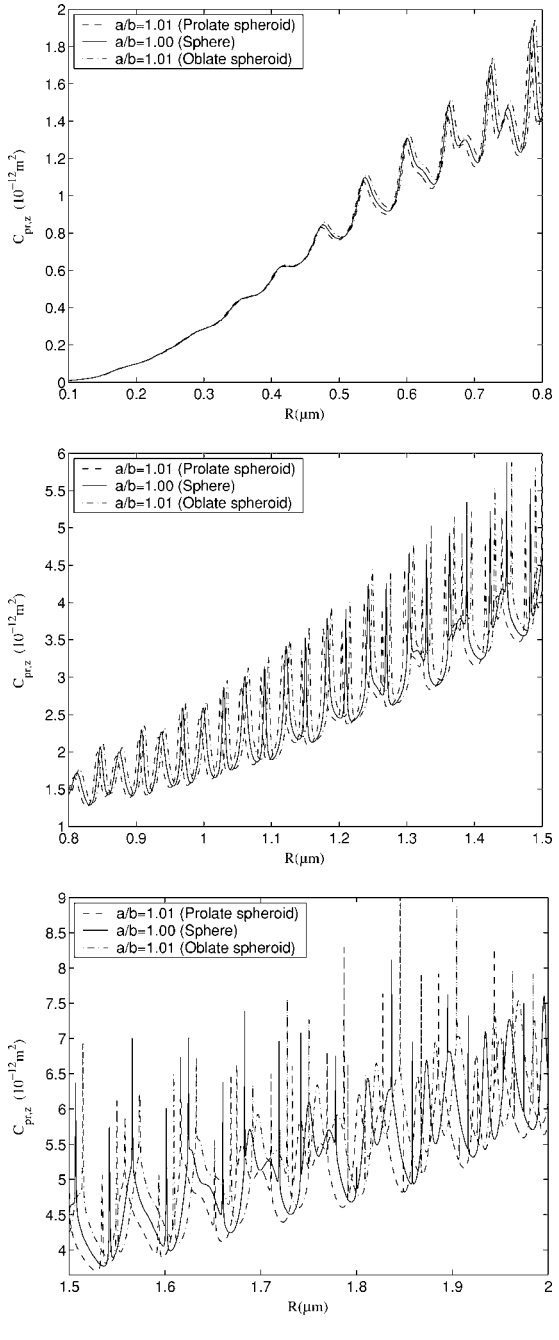

FIG. 3. Comparison of the longitudinal RPCS $C_{\mathrm{pr},z}$ exerted by a plane wave on the spheroid of axis ratio $a/b=1.01$ to that on the sphere. The incidence and polarization angles of the plane wave are assumed to be 0°. The particles have the same relative refractive index $\hat{m}=1.5$. The dashed curve is for the prolate spheroid of semiminor axis length equal to the radius of the projection area ($R=b$) and the dashed-doted curve is for the oblate spheroid of semimajor axis length equal to the radius of the projection area ($R=a$). The results are compared with GLMT radiation pressure predictions for the sphere of radius R. (1) (a) is for 0.1 μm$\leqslant R\leqslant$0.8 μm; (2) (b) is for 0.8 μm$\leqslant R\leqslant$1.5 μm; (3) (c) is for 1.5 μm$\leqslant R\leqslant$2.0 μm.

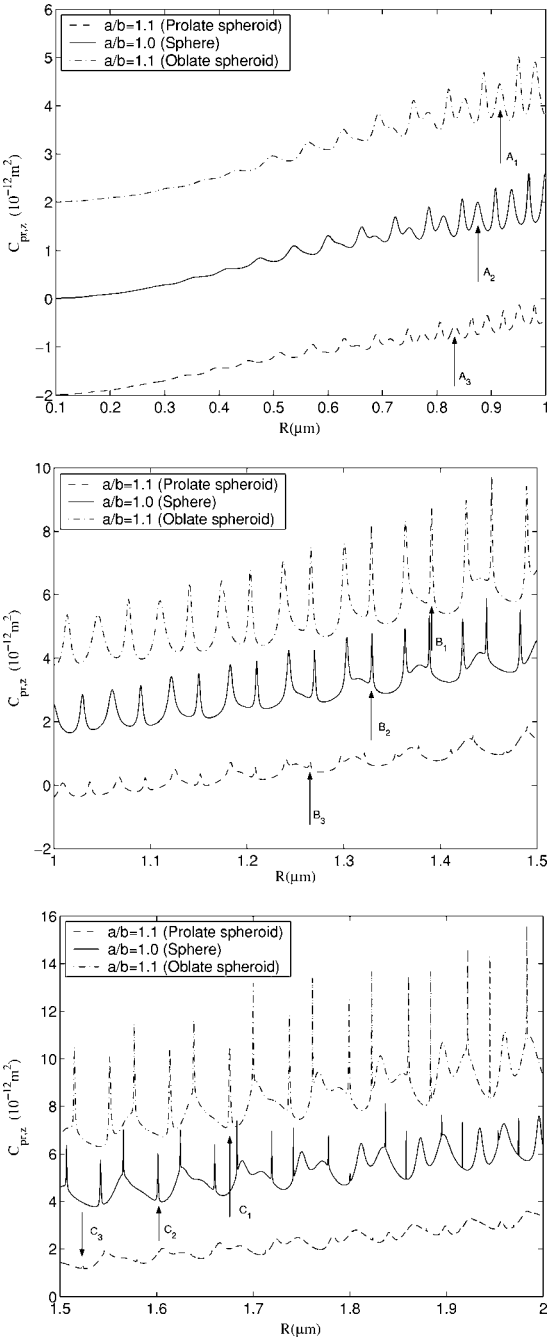

FIG. 4. Same as Fig. 3 but for the axis ratio $a/b=1.1$. (1) (a) is for 0.1 μm$\leqslant R\leqslant$1.0 μm; (2) (b) is for 1.0 μm$\leqslant R\leqslant$1.5 μm; (3) (c) is for 1.5 μm$\leqslant R\leqslant$2.0 μm. For clarity and convenient identification, the RPCS curves of the prolate and oblate spheroids have been offset by the factors 2×10^{-12} and -2×10^{-12}, respectively.

tion of a spherical particle to a spheroidal one. In this way, we numerically simulate the experiment of the "Optical Stretcher" [41] for a RBC acted on by two end-on incident counter-propagating Gaussian beams of TEM_{00} mode. These two beams are identical except for the opposite propagation directions. The RBC is located where beam sections are identical. Provided that the hemoglobin filled in the soft RBC is incompressible, its volume will not change in the process of deformation.

As described in Ref. [41], such a spherical RBC of radius $R=3.32$ μm (volume $V_0=153.3$ μm^3) and refractive index $\hat{m}_2=1.380$ is in a buffer of refractive index $\hat{m}_1=1.335$. A

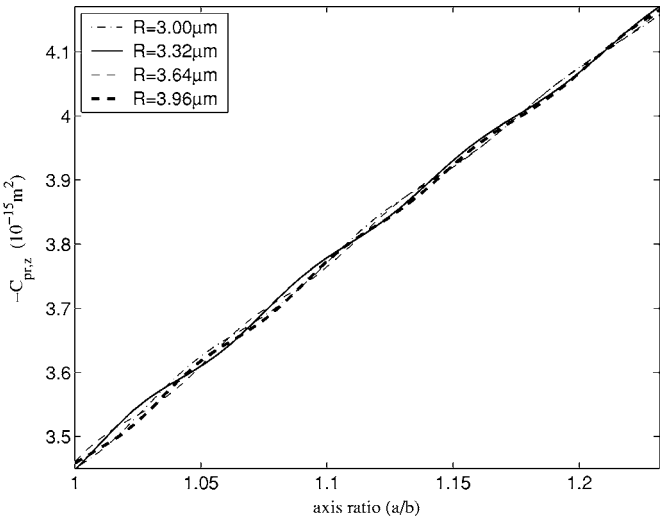

FIG. 5. Longitudinal RPCS versus the axis ratio for a red blood cell (RBC) of radii 3.00, 3.32, 3.64, and 3.96 μm, located on the beam axis with the location characterized by $\omega/R=1.1$. The RBC of refractive index 1.380 is in the buffer of refractive index 1.335, and is deformed from the spherical shape to the spheroidal one under the action of two counter-propagating laser beams in the TEM_{00} mode. The volume of the particle remains constant during the deformation. The circular Gaussian beam has a waist radius $\omega_0=0.5\lambda$. Note that $C_{pr,z}$ plotted in Fig. 5 represents the RPCS of beam *A*, which propagates in the direction of the positive *z* axis. The incidence and polarization angles of the beams are $\Theta_{bd}=\Phi_{bd}=0$. Beam *B*, which has the same axis as beam *A* but opposite propagation direction, has RPCS of the same value as beam *A* but with opposite sign.

cw-Ti: sapphire laser is used to produce the beam of wavelength $\lambda_0=0.785$ μm. The beam is assumed to be extremely focused to the waist radius $\omega_0=0.5\lambda_0$ and its center O_B is located on the *z* axis. The ratio of the local waist radius to the particle radius is 1.10 ($\omega/R=1.10$). We calculate the RPCS for the axis ratio $1.00\leqslant a/b\leqslant 1.23$, corresponding to the linear expansions along the *z* axis of $0\leqslant\Delta z_0\leqslant 0.8$ μm and the linear contraction along the *y* axis of $0\leqslant\Delta y_0\leqslant 0.6$ μm [41]. As indicated by the solid curve in Fig. 5, the longitudinal RPCS, $C_{pr,z}$, presents a linearly increasing relationship with the growth of the axis ratio a/b. Its absolute value rises from 3.45×10^{-15} m^2 for $a/b=1.00$ to 4.17×10^{-15} m^2 for $a/b=1.23$. This means that for an "Optical Stretcher" with a given beam power, the RPF exerted on the RBC will gradually increase by 20% when it is deformed from a sphere to a prolate spheroid of $a/b=1.23$. Since a normal RBC has the radius between 3 μm and 4 μm, in Fig. 5, we also plot the RPCS curves for the RBCs of the radii $R=3.00$ μm, 3.64 μm, and 3.96 μm, respectively. These cells are still assumed to be located at the position $\omega/R=1.1$. Their RPCS curves show a similar increase. Therefore we may suppose that, in the experiment of the "Optical Stretcher" using extremely focused beams, the linear deformation of a spherical RBC is not only the contribution of the beam power increasing but also the contribution of particle shape changing itself during the deformation. Note should be paid to the fact that, for the RBC of radius 3.32 μm, when the linear expansion along the *z* axis ($\Delta z_0=2\Delta a$) increases from 0 to 0.8 μm and the linear contraction along the *y* axis ($\Delta y_0=2\Delta b$) increases from 0 to 0.6 μm (corresponding to $a/b=1.23$), the volume of the particle decreases from the original value $V_0=153.3$ μm^3 to $V_1=142.1$ μm^3, which means the deviation error increasing from 0% to 7.3%. This is contradictory to the constant volume assumption during the deformation and means that the spheroidal model is more appropriate for a slightly deformed RBC. It has been found that [58], when a RBC deviates much from the spherical shape, only its two ends possess the shape partly similar to their counterparts of a spheroid, while the shape of its middle part is more approximate to a cylinder of finite length. Therefore it can be expected that the less a cell deviates from the spherical shape, the better it can be modeled by the spheroid.

C. Radiation pressure force versus incidence and polarization angles

For a sphere, due to its spherical symmetry, once it is located on the beam axis the RPF keeps a constant value in the beam propagation direction for all incidence angles Θ_{bd} and polarization angles Φ_{bd}. However, this is not in general the case for the spheroidal particle due to its unique symmetrical axis along the *z* axis. Further on, at an oblique incidence angle, different polarization angles also imply different ray trajectories inside the spheroid so that the resultant RPF should change accordingly. In this section we exemplify that RPF on a spheroid is affected by both incidence and polarization angles of the beam. When the spheroid with an arbitrary location and orientation in the beam moves toward the beam center O_B, rotation might happen. In this case, we need to evaluate the RPF versus the angles Θ_{bd} and Φ_{bd}, respectively.

First, let a TEM_{00} circular Gaussian beam incident on a prolate spheroid at different incidence angles within [0°, 90°]. Such a range is representative for the characterization of the influence of the incidence angle on the RPF. The RPCS for $90°\leqslant\Theta_{bd}\leqslant 180°$ is identical to its counterpart corresponding to $180°-\Theta_{bd}$ except for an opposite sign for $C_{pr,z}$. And the RPCS for $-180°\leqslant\Theta_{bd}\leqslant 0°$ is identical to its counterpart corresponding to $-\Theta_{bd}$, except for an opposite sign for $C_{pr,x}$. A Gaussian beam of waist radius $\omega_0=2\lambda$ is used for numerical calculations since generally the highly focused beam exerts more RPF on the particle along the beam axis. The polarization angle of the beam is assumed to be 0° ($\Phi_{bd}=0°$). The semiminor axis length and the axis ratio of the spheroid are equal to 0.5 μm and 2.0, respectively. The centers of the beam and the spheroid are assumed to coincide with each other so that O_B has the coordinates $x_0=y_0=z_0=0$ μm in O_P-*xyz*. As can be found in Fig. 6(a), the components of RPCS $C_{pr,z}$ and $C_{pr,x}$ change obviously with the incidence angle Θ_{bd} and have the maxima 3.4×10^{-13} m^2 and 5.6×10^{-13} m^2, respectively, corresponding to the end-on incidence ($\Theta_{bd}=0°$) and side-on incidence ($\Theta_{bd}=90°$) are concerned, respectively. Meanwhile, $C_{pr,z}$ and $C_{pr,x}$ are identical to zero at $\Theta_{bd}=90°$ and 0°, respectively, as it should. The resultant RPCS, which is calculated from $C_{pr,z}$ and $C_{pr,x}$ by $C_{pr,resultant}=\sqrt{C_{pr,x}^2+C_{pr,z}^2}$ ($C_{pr,y}=0$ for the current

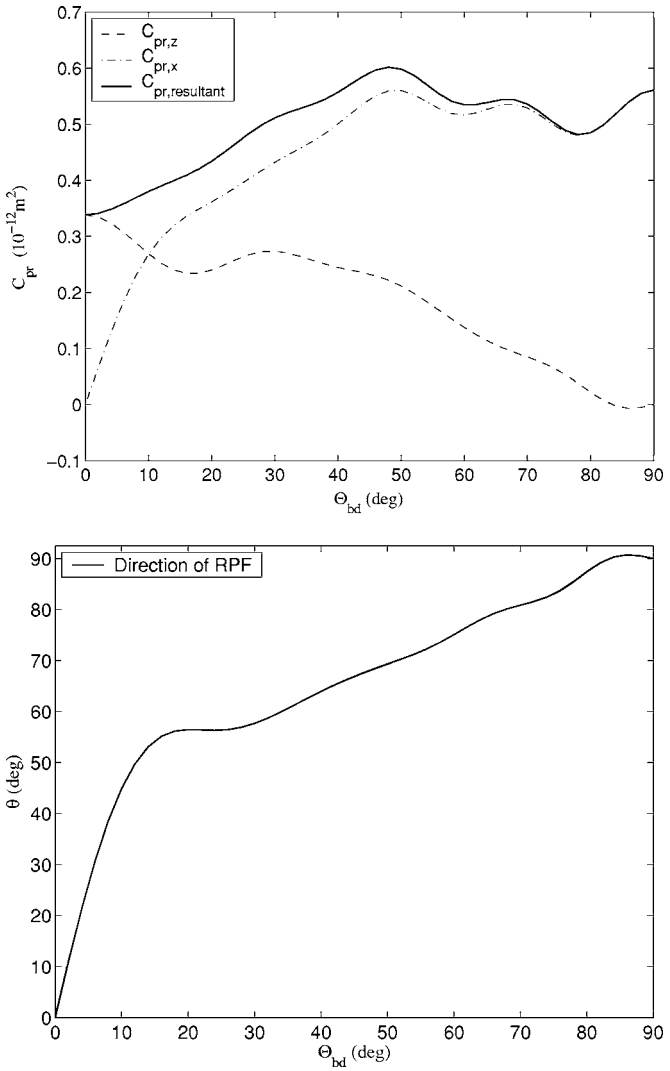

FIG. 6. RPCS versus the incidence angle Θ_{bd}. The polarization angle Φ_{bd} is assumed to be 0. The circular Gaussian beam of the waist radius $\omega_0=2\lambda$ is assumed to illuminate a prolate spheroid of axis ratio $a/b=2.0$, with semiminor axis length $b=0.5$ μm and relative refractive index $\hat{m}=1.5$. Note that $C_{pr,y}$ is equal to zero and hence is curve is not plotted. (1) In (a) is plotted the RPCS curve versus Θ_{bd}, including the longitudinal component of RPCS $C_{pr,z}$, the transverse the $C_{pr,x}$, as well as the resultant one; (2) in (b) is plotted the direction of the resultant RPF ($O_{P\text{-}xy}$ plane) exerted on the spheroid. Note that θ is formed by the direction of the resultant RPF and the positive z axis, while Θ_{bd} is formed by the beam propagation direction and the positive z axis.

case), also changes with the incidence angle and has its maximum 6.0×10^{-13} at $\sim48°$. Thus, we can conclude that the RPF value does not keep constant for the different incidence angles. Neither does its direction, as can be found in Fig. 6(b): except for their equalities for the end-on or side-on incidences of the beam ($\Theta_{bd}=0°$ or 90°), the angle formed by the direction of the RPF and the z axis, θ, is always larger than incidence angle of the beam, Θ_{bd}. As evidenced by other numerical results not demonstrated in the present paper, we comment that the more a spheroid deviates from the sphere, the more the RPCS curve is influenced by the incidence and polarization angles.

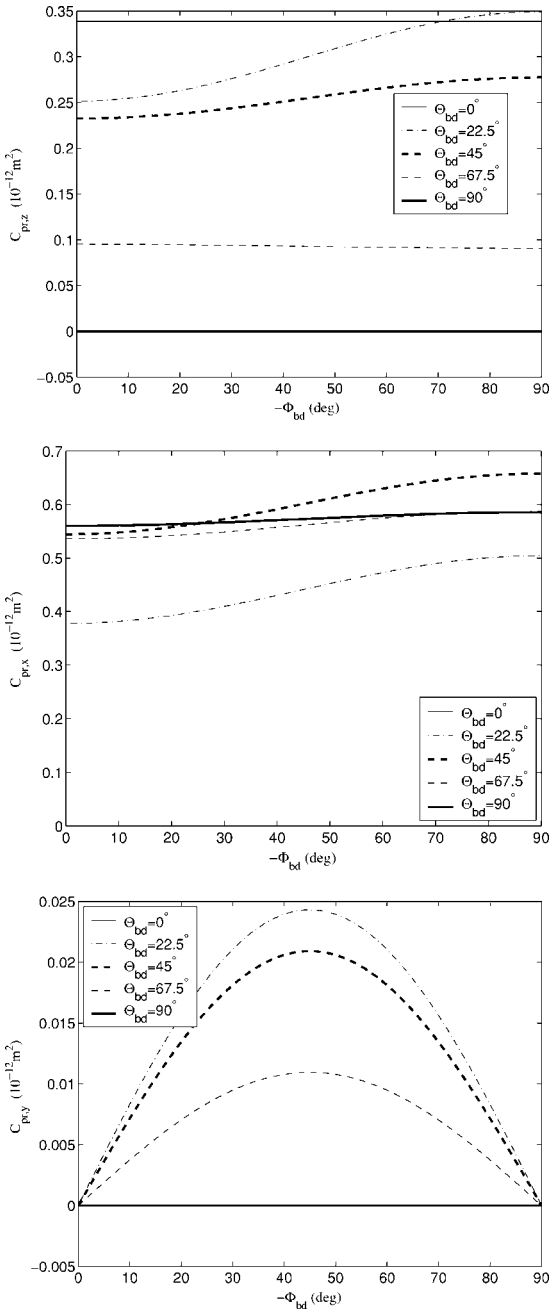

FIG. 7. RPCS versus the polarization angle Φ_{bd} for five incidence angles $\Theta_{bd}=0°$, 22.5°, 45°, 67.5°, and 90°. The beam and the spheroid are the same as in Fig. 6. In (a), (b), and (c) are plotted the curves of $C_{pr,z}$, $C_{pr,x}$, and $C_{pr,y}$ versus Φ_{bd}, respectively. For $\Theta_{bd}=0°$, $C_{pr,x}$, and $C_{pr,y}$ are zero and therefore their curves are not explicitly found in the figures.

Next, using the same particle and beam, we study the influence of the polarization angle on the result of RPCS. For the given incidence angles 0°, 22.5°, 45°, 67.5°, and 90°, the polarization of the incident wave changes from the *TM* mode ($\Phi_{bd}=0°$) to the *TE* mode ($\Phi_{bd}=-90°$). In such a process, the RPCS curves of $C_{pr,z}$, $C_{pr,x}$, and $C_{pr,y}$ versus the polarization angles are illustrated in Figs. 7(a)–7(c), respectively. Evidently, when $\Theta_{bd}=0°$, $C_{pr,z}$ keeps constant for all polarization angles, due to the rotational symmetry of the spheroid

about its semimajor axis. $C_{pr,z}$ becomes zero when the beam is tilted to the incidence angle 90°, since in this case the beam propagates along the x axis in the Cartesian coordinates of the spheroid. For the incidence angle $\Theta_{bd}=22.5°$, $C_{pr,z}$ shows a monotone increasing relationship with the growth of the polarization angle Φ_{bd}. Such a tendency of increasing slows down for $\Theta_{bd}=45°$. When $\Theta_{bd}=67.5°$, the $C_{pr,z}$ curve versus Φ_{bd} becomes monotone decreasing. As to $C_{pr,x}$, it grows gradually with the increase of Φ_{bd} for all incidence angles except when $\Theta_{bd}=0°$, which corresponds to the end-on incidence of the beam when no transverse forces exist. Interestingly enough, the curve of $C_{pr,y}$ presents a parabolic shape for incidence angles $\Theta_{bd}=22.5°$, 45°, and 67.5°. The maximum of $C_{pr,y}$ locates stably at $\Phi_{bd}=-45°$, as can be found in Fig. 7(c). But for the end-on incidence ($\Theta_{bd}=0°$) or side-on incidence ($\Theta_{bd}=90°$), $C_{pr,y}$ is equal to zero at all polarization angles. Considering the ray optics viewpoint, this is because the two geometrical rays at the same polarization plane and symmetrical about the beam axis have symmetrical trajectories inside the particle so that they produce no forces in the y direction. For other incidence angles, $C_{pr,y}$ still keeps zero at the polarization angles $\Phi_{bd}=0°$ and −90°, since in these cases two symmetrical incident rays, respectively, located at the left-hand and right-hand sides of O_P-xz plane can still be found propagating symmetrically inside the spheroid so that eventually no forces are produced in the y direction. However, for a given incidence angle $0° \ll_{bd} < 90°$ and at the other polarization angles $-90° < \Phi_{bd} < 0°$, such a symmetrical propagation does not exist any longer, therefore $C_{pr,y}$ happens to be nonzero.

Note should be paid to the fact that the RPCS for $0° \leqslant \Phi_{bd} \leqslant 90°$ is identical to its counterpart corresponding to $-\Phi_{bd}$. Also, the RPCS for $90° \leqslant \Phi_{bd} \leqslant 180°$ and $-180° \leqslant \Phi_{bd} \leqslant -90°$ is identical to its counterpart corresponding to $-\Phi_{bd}$.

D. RADIATION PRESSURE FORCE VERSUS BEAM CENTER LOCATION

For on-axis location of the spheroid, under the action of the longitudinal RPF the spheroid will be attracted toward the beam center. In such a process, we need to explore the influence of beam center location O_B (x_0, y_0, z_0) on the RPCS. First, we discuss the case of end-on incidence of the beam. In this case, the beam center O_B is located on the z axis so that $x_0=y_0=0$ μm. We consider a Rayleigh particle ($R \ll \lambda$) of $R=0.01$ μm as an example, which is representative of RPCS prediction for Rayleigh particles. For both spherical and spheroidal particles of the same projection radius R and illuminated by an end-on incident circular Gaussian beam of waist radius $\omega_0=\lambda$ and its electric field polarized in O_P-xz plane, the $C_{pr,z}$ curves versus z_0 show a symmetrical shape about the point with $z_0=0$ μm and $C_{pr,z}$ is almost zero, as can be found in Fig. 8. Meanwhile, the absolute value of longitudinal RPCS ($|C_{pr,z}|$) of the oblate and/or prolate spheroid is smaller and/or larger than that of the sphere and increases and/or decreases with the growth of the axis ratio from 1.0 to 1.2. (These axis ratios can be looked on as caused by an "Optical Stretcher," which is discussed in Sec. III B.) Such a phenomenon is observed for all particles within the Rayleigh size range. However, it is not always the case for particles of size beyond the Rayleigh region. For example, when $R=1.0$ μm, $|C_{pr,z}|$ at almost all z_0 decreases with the growth of the axis ratios from 1.0 to 1.10, as indicated by Fig. 9. Also, at relatively far location of the beam center O_B from the particle center O_P (say, $|z_0|>20$ μm), the curvatures of the beam wavefronts at $+|z_0|$ and $-|z_0|$, which

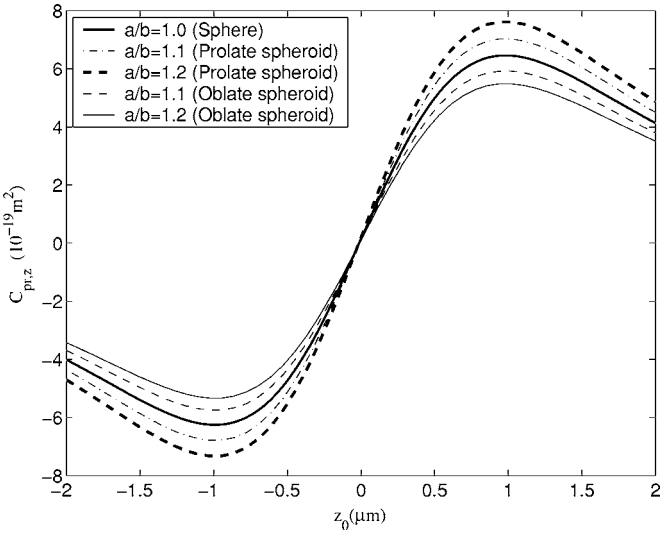

FIG. 8. Longitudinal RPCS versus the location of Rayleigh particle along the z axis. The circular Gaussian beam has a waist radius $\omega_0=\lambda$. The spheroids have the relative refractive index $\hat{m}=1.5$ but different axis ratios $a/b=1.1$ and 1.2, respectively. The projection radius of the particles is assumed to be $R=0.01$ μm so that we have $R=b$ for the prolate spheroid and $R=a$ for the oblate one. The incidence and polarization angles of the beams are $\Theta_{bd}=\Phi_{bd}=0$.

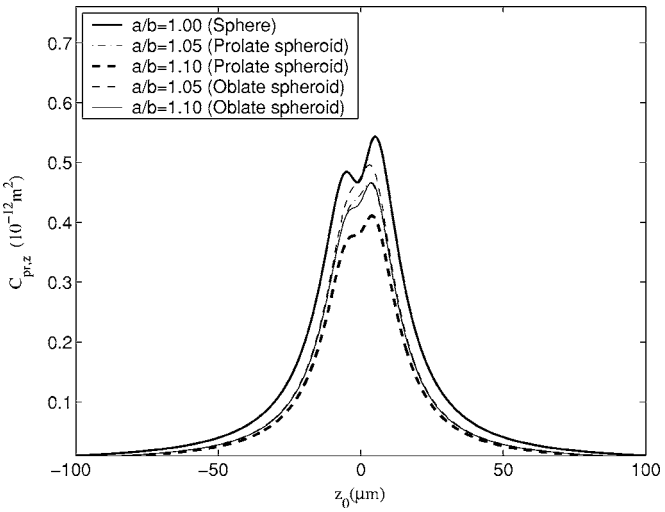

FIG. 9. Longitudinal RPCS versus particle location along the z axis. The circular Gaussian beam has a waist radius $\omega_0=2\lambda$. The spheroids have the same relative refractive index $\hat{m}=1.5$ but the different axis ratios $a/b=1.05$ and 1.10, respectively. The projection radius of the particles is assumed to be $R=1.0$ μm so that we have $R=b$ for the prolate spheroid and $R=a$ for the oblate one. The incidence and polarization angles of the beams are $\Theta_{bd}=\Phi_{bd}=0$.

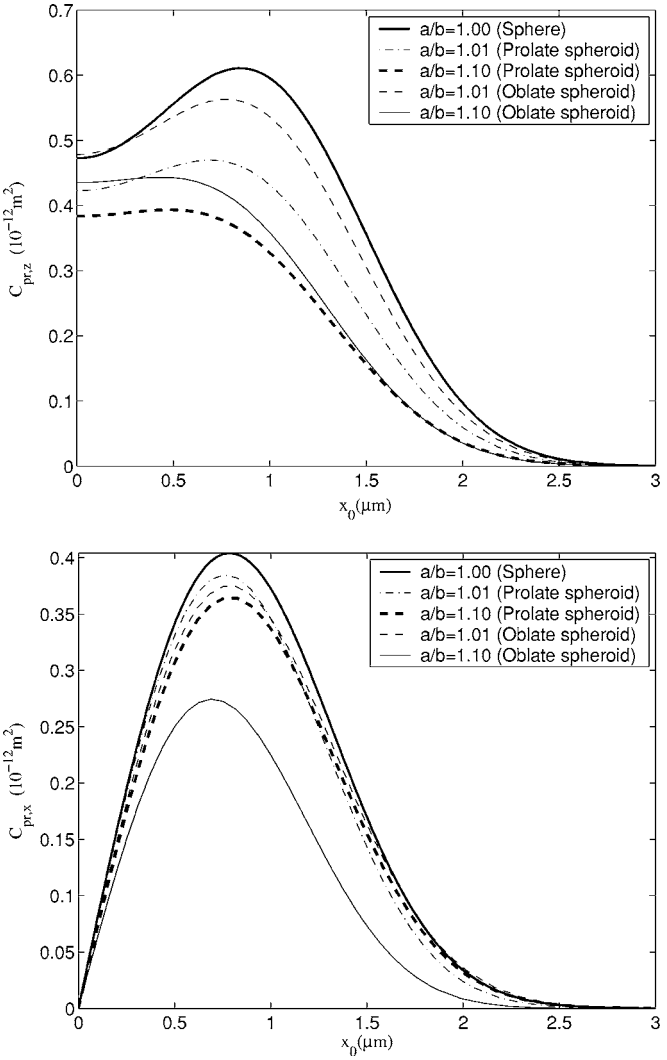

FIG. 10. Transverse RPCS $C_{pr,x}$ versus the beam center location along the positive x axis. The circular Gaussian beam of a waist radius $\omega_0=2\lambda$ is assumed to be incident on spheroids of the same relative refractive index $\hat{m}=1.5$ but with different axis ratios $a/b=1.00$, 1.01, and 1.10, respectively. The beam center locates on the x axis so that $y_0=z_0=0$ μm. The incidence and polarization angles of the beam are $\Theta_{bd}=\Phi_{bd}=0$. The projection radius of the particle is $R=1.0$ μm. (1)(a) is for the longitudinal RPCS $C_{pr,z}$ versus x_0; and (2)(b) is for the transverse RPCS $C_{pr,x}$ versus x_0. Attention should be paid to the fact that, in the current case, another transverse RPCS, $C_{pr,y}$, is zero and its curve is not plotted.

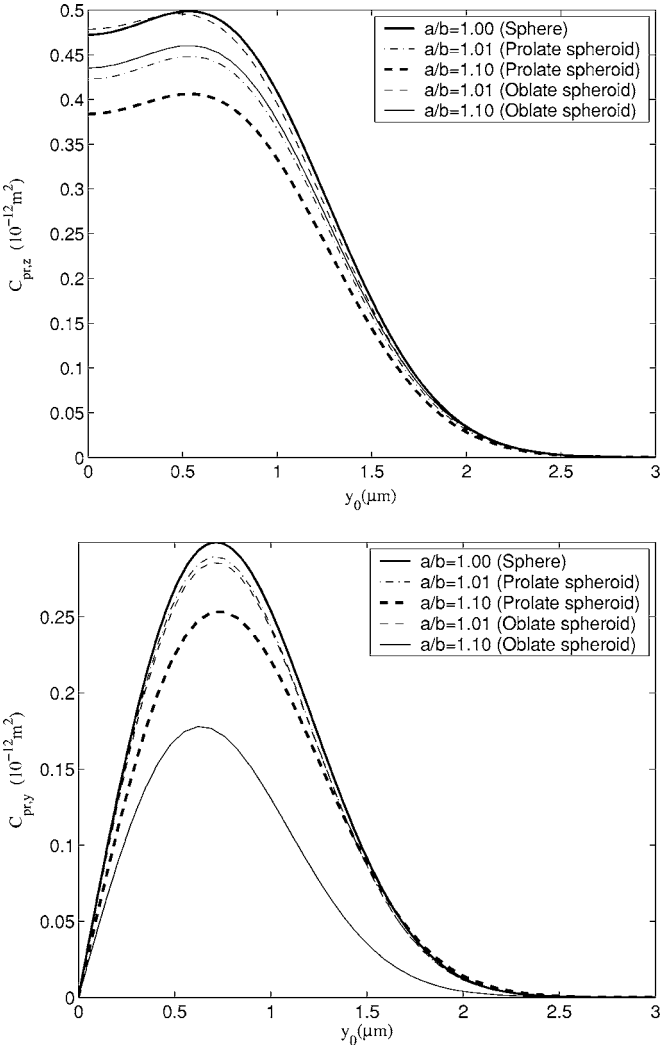

FIG. 11. Same as Fig. 10 but for the transverse RPCS $C_{pr,y}$ versus the beam center location along the positive y axis. The beam center O_B locates on the positive y axis so that $x_0=z_0=0$ μm. (1) (a) is for the longitudinal RPCS $C_{pr,z}$ versus y_0; and (2) (b) is for the transverse RPCS $C_{pr,y}$ versus y_0. Attention should be paid to the fact that, in the current case, another transverse RPCS, $C_{pr,x}$, is zero and its curve is not plotted.

correspond to the particle located at the converging or diverging parts of the beam, respectively, are weak enough to be looked on as being identical. Therefore a symmetry of the $C_{pr,z}$ curve is found with respect to the axis $z_0=0$ μm. Next, we discuss the case of off-axis incidence of the beam for the spheroid located in a cross section of the beam center O_B with $z_0=0$ but $x_0\neq 0$ or $y_0\neq 0$. A circular Gaussian beam of waist radius $\omega_0=2\lambda$, with the incidence and polarization angles $\Theta_{bd}=\Phi_{bd}=0$ illuminates spheroids having the same projection radius $R=1.0$ μm but the different axis ratios $a/b=1.00$, 1.01, and 1.10. Since the beam center is located along the x axis, we have $y_0=z_0=0$ μm. In this case, the longitudinal and the transverse RPCS curves, $C_{pr,z}$ and $C_{pr,x}$ versus x_0, are plotted in Fig. 10(a) and Fig. 10(b), respectively. Also, for the beam center located along the y axis ($x_0=z_0=0$ μm), results of $C_{pr,z}$ and $C_{pr,y}$ are plotted in Fig. 11(a) and Fig. 11(b). We can find from Fig. 10(a) and Fig. 11(a) that, for the same projection radius $R=1.0$ μm the longitudinal pressures exerted on the spheroids of axis ratio $a/b\leqslant 1.1$ are less than those exerted on the sphere when the beam center O_B is not close enough to the particle center O_P, say $x_0\geqslant 0.32$ μm for $C_{pr,x}$ and $y_0\geqslant 0.40$ μm for $C_{pr,y}$. Meanwhile, as indicated by Fig. 10(b) and Fig. 11(b), the transverse pressures exerted on the spheroids are less than those exerted on the sphere once the beam center does not locate far enough from the particle center, say $0\leqslant x_0\leqslant 1.75$ μm for $C_{pr,x}$ and $0\leqslant y_0\leqslant 1.65$ μm for $C_{pr,y}$.

When the volatile oil is polluted or contains some impurities, the refractive index might have a nonzero imaginary part. In this case, the influence of the refractive index on

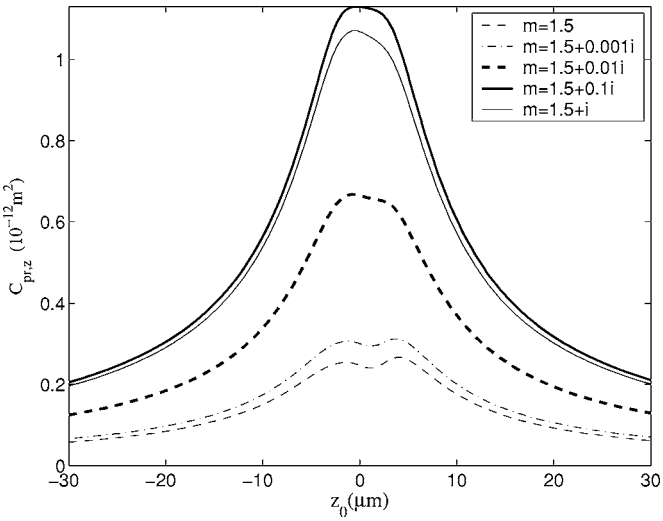

FIG. 12. Longitudinal RPCS versus z_0 for a prolate spheroid of axis ratio $a/b=1.5$ and semiminor axis length $b=1.0$ μm illuminated by an astigmatic elliptical Gaussian beam of waist radii along u and v directions being λ and 10λ, respectively ($\omega_{0u}=\lambda$ and $\omega_{0v}=10\lambda$). The locations of the waist radii ω_{0u} and ω_{0v} are −0.5 μm and 0.5 μm, respectively ($w_u=-0.5$ μm and $w_v=0.5$ μm). The incidence and polarization angles of the beam are $\Theta_{bd}=\Phi_{bd}=0$. The five curves correspond to spheroids of different refractive indices $\hat{m}=1.5$, $1.5+0.001i$, $1.5+0.01i$, $1.5+0.1i$, and $1.5+i$.

RPCS should be examined. We use an astigmatic elliptical Gaussian beam [56] of waist radii along u and v directions being λ and 10λ, respectively ($\omega_{0u}=\lambda$ and $\omega_{0v}=10\lambda$). The locations of the waist radii along the u and v axes are −0.5 μm and 0.5 μm, respectively ($w_u=-0.5$ μm and $w_v=0.5$ μm). The beam is assumed to be incident on a prolate spheroid of axis ratio $a/b=1.5$ and semiminor axis length $b=1.0$ μm. The real part of the refractive index of the prolate spheroids is 1.5 [$\mathrm{Re}(\hat{m})=1.5$] and its imaginary part $\mathrm{Im}(\hat{m})$ grows from 0 to 0.1 by steps. For these parameters, we observe a gradual increase of the $C_{pr,z}$ curve in Fig. 12. However, when $\mathrm{Im}(\hat{m})$ further grows to 1.0, a decrease is observed. Since the influence of the imaginary part of the refractive index on the behavior of the RPCS curves versus z_0 has been found similar to the one for the C_{abs} curves, the explanation can be as follows: when more (less) energy is absorbed by the particle, more (less) angular momentum is transferred to the particle so that the longitudinal RPCS becomes larger (smaller).

IV. CONCLUSION

A rigorous theory is developed for calculating the radiation pressure force exerted on a spheroidal particle. The incident beam can be of arbitrary shape, exhibiting known expressions of electromagnetic fields in Cartesian coordinates of the spheroid, so that it can be expanded in the associated spheroidal coordinates and described by a set of beam shape coefficients $(G^m_{n,TE}, G^m_{n,TM})$. Numerical calculations are performed for both prolate and oblate spheroids illuminated by plane wave or circular and/or elliptical Gaussian beam. To study the influence of particle shape on the RPF, the results of RPCS of the spheroids are compared to those of the spheres. For the plane wave incidence, the RPCS curve versus the particle size for a prolate spheroid has a backward and downward shift when compared to the RPCS curve for a sphere. Such a shift becomes upward and forward for an oblate spheroid of the same axis ratio as that of the prolate one. Moreover, the resonance strength of the oblate and/or prolate spheroid is stronger and/or weaker than that of the sphere. Also, when the particle is located on the beam axis, the resultant RPF exerted on the spheroid, unlike on the sphere, is not always along the beam propagation direction denoted by the incidence angle Θ_{bd}. Furthermore, its value does not remain constant. Besides, altering the polarization angle can also bring changes to the RPF for a beam of oblique incidence ($\Theta_{bd}\neq 0°$). By use of the present theory, our numerical simulation of the "Optical Stretcher" indicates that, during the deformation of a RBC acted on by two extremely focused TEM_{00} beams with $\omega_0=0.5\lambda$ and given beam power, the longitudinal RPF exerted on the cell with its location in the beam characterized by $\omega/R=1.1$ linearly increases by 20% when it is deformed from a spherical particle to a spheroidal one having an axis ratio $a/b=1.23$.

ACKNOWLEDGMENTS

The authors acknowledge support from the French Embassy in China (Contract No. 4B2-007) and from the Natural Science Foundation of China (Grant No. 50336050).

APPENDIX

The orthogonality relation for exponentials $\exp(ip\phi)$ is [47]

$$\int_0^{2\pi} \exp[i(p-p')\phi]d\phi = 2\pi\delta_{pp'}. \tag{A1}$$

If we denote τ_n^m and π_n^m as the generalized Legendre functions of Ferrer's definition as follows [46]:

$$\tau_n^p = \frac{dP_n^p(\cos\theta)}{d\theta}, \tag{A2}$$

$$\pi_n^p = \frac{P_n^p(\cos\theta)}{\sin\theta}, \tag{A3}$$

four orthogonality relations used in the RPF calculation for a spherical particle have been found as follows [26]:

$$I_3 = \int_0^{\pi} (\tau_n^{|p|}\tau_{n'}^{|p|} + p^2\pi_n^{|p|}\pi_{n'}^{|p|})\sin\theta\cos\theta d\theta$$

$$= \frac{2(n-1)(n+1)(n+|p|)!}{(2n-1)(2n+1)(n-|p|-1)!}\delta_{n',n-1}$$

$$+ \frac{2(n'-1)(n'+1)(n'+|p|)!}{(2n'-1)(2n'+1)(n'-|p|-1)!}\delta_{n,n'-1}, \tag{A4}$$

$$I_4 = \int_0^{\pi} (\tau_n^{|p|}\pi_{n'}^{|p|} + \tau_{n'}^{|p|}\pi_n^{|p|})\sin\theta\cos\theta d\theta = \frac{2(n+|p|)!}{(2n+1)(n-|p|)!}\delta_{nn'}, \tag{A5}$$

$$I_5 = \int_0^{\pi} [\tau_n^{|p|}\tau_{n'}^{|p+1|} + p(p+1)\pi_n^{|p|}\pi_{n'}^{|p+1|}]\sin^2\theta d\theta$$
$$= \begin{cases} -\dfrac{2}{(2n+1)(2n'+1)}\dfrac{(n'+|p|+1)!}{(n'-|p|-1)!}[(n-1)(n+1)\delta_{n,n'+1} - (n'-1)(n'+1)\delta_{n',n+1}], & p \geqslant 0, \\ -\dfrac{2}{(2n+1)(2n'+1)}\dfrac{(n-|p|)!}{(n+|p|)!}[(n'-1)(n'+1)\delta_{n',n+1} - (n-1)(n+1)\delta_{n,n'+1}], & p < 0, \end{cases} \tag{A6}$$

$$I_6 = \int_0^{\pi} [p\pi_n^{|p|}\tau_{n'}^{|p+1|} + (p+1)\pi_{n'}^{|p+1|}\tau_n^{|p|}]\sin^2\theta d\theta = \begin{cases} -\dfrac{2}{(2n+1)}\dfrac{(n+|p|+1)!}{(n-|p|-1)!}\delta_{nn'}, & p \geqslant 0, \\ \dfrac{2}{(2n+1)}\dfrac{(n-|p|)!}{(n+|p|)!}\delta_{nn'}, & p < 0. \end{cases} \tag{A7}$$

Since the spheroidal angular functions $S_{pn}(c_{\mathrm{I}},\cos\theta)$ can be written as infinite series of the Legendre functions $P_n^p(\cos\theta)$ as follows [48]:

$$S_{pn}(c_{\mathrm{I}},\cos\theta) = \sum_{r=0,1}^{\infty}{}' d_r^{|p|n}(c_{\mathrm{I}})P_{|p|+r}^{|p|}(\cos\theta), \tag{A8}$$

after some mathematical algebra, $J_{nn'}^p - M_{nn'}^p$, the four orthogonality relations corresponding to $I_3 - I_6$ but for S_{pn} and S'_{pn} can also be obtained,

$$J_{nn'}^p = \int_0^{\pi} \left(\frac{dS_{|p|n}(c_{\mathrm{I}},\cos\theta)}{d\theta}\frac{dS_{|p|n'}(c_{\mathrm{I}},\cos\theta)}{d\theta} + p^2\frac{S_{|p|n}(c_{\mathrm{I}},\cos\theta)}{\sin\theta}\frac{S_{|p|n'}(c_{\mathrm{I}},\cos\theta)}{\sin\theta} \right)\sin\theta\cos\theta d\theta$$
$$= \begin{cases} \displaystyle\sum_{r=2,1}^{\infty}{}' \frac{2(|p|+r-1)(|p|+r+1)}{(2|p|+2r-1)(2|p|+2r+1)}\frac{(2|p|+r)!}{(r-1)!}d_r^{|p|n}d_{r-1}^{|p|n'} \\ \quad + \displaystyle\sum_{r=0,1}^{\infty}{}' \frac{2(|p|+r)(|p|+r+2)}{(2|p|+2r+1)(2|p|+2r+3)}\frac{(2|p|+r+1)!}{r!}d_r^{|p|n}d_{r+1}^{|p|n'}, & |n-n'| = \text{odd}, \\ 0, & |n-n'| = \text{even}, \end{cases} \tag{A9}$$

$$K_{nn'}^p = \int_0^{\pi} \left(\frac{dS_{|p|n}(c_{\mathrm{I}},\cos\theta)}{d\theta}\frac{S_{|p|n'}(c_{\mathrm{I}},\cos\theta)}{\sin\theta} + \frac{dS_{|p|n'}(c_{\mathrm{I}},\cos\theta)}{d\theta}\frac{S_{|p|n}(c_{\mathrm{I}},\cos\theta)}{\sin\theta} \right)\sin\theta\cos\theta d\theta$$
$$= \begin{cases} 0, & |n-n'| = \text{odd}, \\ \displaystyle\sum_{r=0,1}^{\infty}{}' \frac{2}{(2|p|+2r+1)}\frac{(2|p|+r)!}{r!}d_r^{|p|n}d_r^{|p|n'}, & |n-n'| = \text{even}, \end{cases} \tag{A10}$$

$$L_{nn'}^{p}=\int_{0}^{\pi}\left(\frac{dS_{|p|n}(c_{\mathrm{I}},\cos\theta)}{d\theta}\frac{dS_{|p+1|n'}(c_{\mathrm{I}},\cos\theta)}{d\theta}+p(p+1)\frac{S_{|p|n}(c_{\mathrm{I}},\cos\theta)}{\sin\theta}\frac{S_{|p+1|n'}(c_{\mathrm{I}},\cos\theta)}{\sin\theta}\right)\sin^{2}\theta d\theta$$

$$=\begin{cases}-\left(\sum_{r=2,3}^{\infty}{}'\frac{2(|p|+r-1)(|p|+r+1)}{(2|p|+2r-1)(2|p|+2r+1)}\frac{(2|p|+r)!}{(r-2)!}d_{r}^{|p|n}d_{r-2}^{|p+1|,n'}\right.\\ \left.\quad-\sum_{r=0,1}^{\infty}{}'\frac{2(|p|+r)(|p|+r+2)}{(2|p|+2r+1)(2|p|+2r+3)}\frac{(2|p|+r+2)!}{r!}d_{r}^{|p|n}d_{r}^{|p+1|,n'}\right), & |n-n'|=\text{odd},\quad p\geqslant 0\\ -\left(\sum_{r=0,1}^{\infty}{}'\frac{2(|p|+r)(|p|+r+2)}{(2|p|+2r+1)(2|p|+2r+3)}\frac{(2|p|+r)!}{r!}d_{r}^{|p|n}d_{r+2}^{|p-1|,n'}\right.\\ \left.\quad-\sum_{r=0,1}^{\infty}{}'\frac{2(|p|+r-1)(|p|+r+1)}{(2|p|+2r-1)(2|p|+2r+1)}\frac{(2|p|+r)!}{r!}d_{r}^{|p|n}d_{r}^{|p-1|,n'}\right), & |n-n'|=\text{odd},\quad p<0,\\ 0, & |n-n'|=\text{even},\end{cases}\tag{A11}$$

$$M_{nn'}^{p}=\int_{0}^{\pi}\left(p\frac{S_{|p|n}(c_{\mathrm{I}},\cos\theta)}{\sin\theta}\frac{dS_{|p+1|n'}(c_{\mathrm{I}},\cos\theta)}{d\theta}+(p+1)\frac{S_{|p+1|n'}(c_{\mathrm{I}},\cos\theta)}{\sin\theta}\frac{dS_{|p|n}(c_{\mathrm{I}},\cos\theta)}{d\theta}\right)\sin^{2}\theta d\theta$$

$$=\begin{cases}0, & |n-n'|=\text{odd},\\ -\sum_{r=2,1}^{\infty}{}'\frac{2}{2|p|+2r+1}\frac{(2|p|+r+1)!}{(r-1)!}d_{r}^{|p|n}d_{r-1}^{|p+1|,n'}, & |n-n'|=\text{even},\quad p\geqslant 0,\\ \sum_{r=0,1}^{\infty}{}'\frac{2}{2|p|+2r+1}\frac{(2|p|+r)!}{r!}d_{r}^{|p|n}d_{r+1}^{|p-1|,n'}, & |n-n'|=\text{even},\quad p<0.\end{cases}\tag{A12}$$

[1] A. Ashkin, Phys. Rev. Lett. **24**, 156 (1970).
[2] A. Ashkin, Science **210**, 1081 (1980).
[3] A. Ashkin and J. M. Dziedzic, Science **235**, 1517 (1987).
[4] A. Ashkin, J. M. Dziedzic, and T. Yamane, Nature (London) **330**, 769 (1987).
[5] A. Ashkin and J. M. Dziedzic, Proc. Natl. Acad. Sci. U.S.A. **86**, 7914 (1989).
[6] M. J. Lang and S. M. Block, Am. J. Phys. **71**, 201 (2003).
[7] K. C. Neuman and S. M. Block, Rev. Sci. Instrum. **75**, 2787 (2004).
[8] G. Roosen and C. Imbert, Phys. Lett. **59A**, 6 (1976).
[9] G. Roosen, Opt. Commun. **21**, 189 (1977).
[10] G. Roosen and S. Slansky, Opt. Commun. **29**, 341 (1979).
[11] T. C. B. Schut, G. Hesselink, B. G. Grooth, and J. Greve, Cytometry **12**, 479 (1991).
[12] A. Ashkin, Biophys. J. **61**, 569 (1992).
[13] R. Gussgard, T. Lindmo, and I. Brevik, J. Opt. Soc. Am. A **9**, 1922 (1992).
[14] W. H. Wright, G. J. Sonek, and M. W. Berns, Appl. Phys. Lett. **63**, 715 (1993).
[15] W. H. Wright, G. J. Sonek, and M. W. Berns, Appl. Opt. **33**, 1735 (1994).
[16] T. Wohland, A. Rosin, and E. H. K. Stelzer, Optik (Stuttgart) **102**, 181 (1996).
[17] S. Nemoto and H. Togo, Appl. Opt. **37**, 6386 (1998).
[18] M. Gu, P. C. Ke, and X. S. Gan, Rev. Sci. Instrum. **68**, 3666 (2004).
[19] Y. Harada and T. Asakura, Opt. Commun. **124**, 529 (1996).
[20] T. Tlusty, A. Meller, and R. Bar-Ziv, Phys. Rev. Lett. **81**, 1738 (1998).
[21] P. C. Chaumet and M. Nieto-Vesperinas, Opt. Lett. **25**, 1065 (2000).
[22] P. C. Chaumet and M. Nieto-Vesperinas, Phys. Rev. B **61**, 14119 (2000).
[23] A. Rohrbach and E. H. K. Stelzer, J. Opt. Soc. Am. A **18**, 839 (2001).
[24] J. S. Kim and S. S. Lee, J. Opt. Soc. Am. **73**, 303 (1983).
[25] J. P. Barton, J. Appl. Phys. **64**, 1632 (1988).
[26] G. Gouesbet, B. Maheu, and G. Gréhan, J. Opt. Soc. Am. A **5**, 1427 (1988).
[27] H. Polaert, G. Gréhan, and G. Gouesbet, Opt. Commun. **155**, 169 (1998).
[28] J. A. Lock, Appl. Opt. **43**, 2532 (2004).
[29] J. A. Lock, Appl. Opt. **43**, 2545 (2004).
[30] R. C. Gauthier, J. Opt. Soc. Am. B **14**, 3323 (1997).
[31] R. C. Gauthier, J. Opt. Soc. Am. B **14**, 782 (1997).
[32] R. C. Gauthier, Appl. Phys. Lett. **67**, 2269 (1995).
[33] R. C. Gauthier, Appl. Phys. Lett. **69**, 2015 (1996).
[34] Y. Tadir, W. H. Wright, O. Vafa, T. Ord, R. H. Asch, and M. W. Berns, Fertil. Steril. **52**, 870 (1989).
[35] A. Rosse, Biophotonics Int. **17**, 18 (1995).
[36] S. Sato *et al.*, Electron. Lett. **27**, 1831 (1991).

[37] R. W. Steubing, S. Cheng, W. H. Wright, Y. Numajiri, and M. W. Berns, Cytometry **12**, 505 (1991).
[38] J. Z. Zhang and R. K. Chang, Opt. Lett. **13**, 916 (1988).
[39] H. M. Lai, P. T. Leung, K. L. Poon, and K. Young, J. Opt. Soc. Am. B **6**, 2430 (1989).
[40] J. M. Hartings, X. Pu, J. L. Cheung, and R. K. Chang, J. Opt. Soc. Am. B **14**, 2842 (1997).
[41] J. Guck, R. Ananthakrishnan, T. J. Moon, C. C. Cunningham, and J. Käs, Phys. Rev. Lett. **84**, 5451 (2000).
[42] S. Asano and G. Yamamoto, Appl. Opt. **14**, 29 (1975).
[43] J. P. Barton, Appl. Opt. **34**, 5542 (1995).
[44] Y. P. Han and Z. Wu, Appl. Opt. **40**, 2501 (2001).
[45] Y. P. Han *et al.*, Appl. Opt. **42**, 6621 (2003).
[46] F. Xu, K. F. Ren, G. Gouesbet, G. Gréhan, and X. Cai, J. Opt. Soc. Am. A **24**, 119 (2007).
[47] G. Arfken, *Mathematical Methods for Physicists* (Academic, Orlando, 1985).
[48] C. Flammer, *Spheroidal Wave Functions* (Stanford University Press, Stanford, CA, 1957).
[49] C. F. Bohren and D. R. Huffman, *Light Scattering by Small Particles* (Wiley, New York, 1983).
[50] A. Ashkin and J. M. Dziedzic, Phys. Rev. Lett. **38**, 1351 (1977).
[51] A. Ashkin, Phys. Rev. Lett. **24**, 156 (1970).
[52] K. F. Ren, G. Gréhan, and G. Gouesbet, Appl. Opt. **35**, 2702 (1996).
[53] L. W. Davis, Phys. Rev. A **19**, 1177 (1979).
[54] K. F. Ren, G. Gouesbet, and G. Gréhan, Appl. Opt. **37**, 4218 (1998).
[55] G. Gouesbet, J. Opt. Soc. Am. A **16**, 1641 (1999).
[56] F. Xu, K. F. Ren, and X. Cai, J. Opt. Soc. Am. A **24**, 109 (2007).
[57] G. Gouesbet, C. Letellier, K. F. Ren, and G. Gréhan, Appl. Opt. **35**, 1537 (1996).
[58] J. Guck, R. Ananthakrishnan, H. Mahmood, T. J. Moon, C. C. Cunningham, and J. Käs, Biophys. J. **81**, 767 (2001).